Easily Controlled Grafting of Oligonucleotides on γFe2O3 Nanoparticles: Physico-Chemical Characterization of DNA Organization and Biological Activity Studies.

5 AUTHORS, INCLUDING:

Frederic Geinguenaud
Université Paris 13 Nord
18 PUBLICATIONS **151** CITATIONS

SEE PROFILE

Inès Souissi
Atomic Energy and Alternative Energies Com…
6 PUBLICATIONS **96** CITATIONS

SEE PROFILE

Remi Fagard
French Institute of Health and Medical Research
90 PUBLICATIONS **2,071** CITATIONS

SEE PROFILE

Yoann Lalatonne
Université Paris 13 Nord
53 PUBLICATIONS **860** CITATIONS

SEE PROFILE

Easily Controlled Grafting of Oligonucleotides on γFe_2O_3 Nanoparticles: Physicochemical Characterization of DNA Organization and Biological Activity Studies

Frédéric Geinguenaud,[†] Inès Souissi,[‡] Rémi Fagard,[‡,§] Yoann Lalatonne,[†,§] and Laurence Motte*[,†]

[†]Université Paris 13, Sorbonne Paris Cité, Laboratoire CSPBAT, CNRS, (UMR 7244), F-93017, Bobigny, France
[‡]Université Paris 13, Sorbonne Paris Cité, INSERM (U 978), F-93017, Bobigny, France
[§]APHP, Hosp. Avicenne, F-93009, Bobigny, France

S *Supporting Information*

ABSTRACT: We report a one-step process to functionalize superparamagnetic iron oxide nanoparticle (SPIO-NP) surfaces with a controlled number of oligonucleotides. For this study, we use a specific oligonucleotide targeting the signal transducer and activator of transcription 3 (STAT3), a key regulator of cell survival and proliferation. This oligonucleotide is self-complementary and can adopt a hairpin structure. It is labeled with the fluorescein amidite group at the 3′-end. The polyanionic DNA is electrostatically attracted onto the positively charged surface of the bare SPIO-NPs. During synthesis, the molar ratio between the oligonucleotides and nanoparticles was varied from 17.5 to 175. For particles with a mean diameter of 10 nm, a nanoparticle surface saturation is observed corresponding to 70 DNA strands per particle. The increase of DNA density per nanoparticle is correlated to a transition from the hairpin structure adsorbed horizontally on the nanoparticle surface to a vertically ordered surface packing assembly. An in vitro study on human colon carcinoma cell line SW480 shows that the kinetics of internalization and biological activity of the NPs seem to be dependent on the oligonucleotide density. Cell death and the kinetics of internalization are favored by a low density of oligonucleotides.
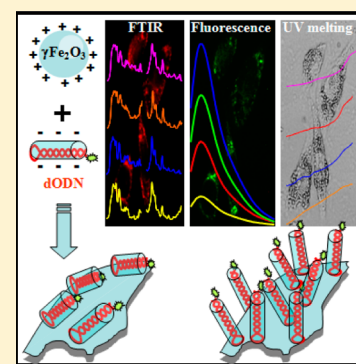
1. INTRODUCTION

During the 1990s, improvements in the synthesis of nucleic acids and suggestions that oligonucleotides might be used to treat a host of diseases, from neurological disorders to cancer, led to an increased use of these potentially therapeutic agents. Most recently, a new interest in RNA therapeutics was raised with the discovery of siRNA. Another strategy is to use a decoy DNA sequence targeting transcription factors. However, a major limitation in the use of nucleic acids is their inability to enter cells on their own. This is because they are subject to degradation by serum nucleases, and because of their negative charge and high hydrophilicity, they are unable to traverse the cell membrane.[1−7]

Even if viral vectors are highly efficient for gene delivery, their design must address many considerations of safety, scale-up procedures, and, in some cases, biological activity. These drawbacks have encouraged the investigation of alternative delivery systems, such as cationic lipids, polymers, and nanoparticles as transport vectors.[8]

In a previous paper,[9] we described a direct, one-step complexation of a labeled decoy oligonucleotide (dODN) with superparamagnetic iron oxide nanoparticles (SPIO-NPs) surfaces decreasing synthesis intermediates and derivatives. This nanoparticle-dODN bioconjugate (SPIO-NP@dODN) was designed to target the signal transducer and activator of transcription 3 (STAT3), a key regulator of cell survival and

proliferation. Constitutive STAT3 activation is involved frequently in uncontrolled tumor cell proliferation; therefore, it constitutes a valuable target for antitumor therapy.[10−13]

In this work, we show that the average number of dODNs per nanoparticle could be controlled and that this is correlated to a transition from the hairpin structure adsorbed horizontally on the nanoparticle surface to a vertically ordered surface packing assembly. The nanocomplexes were incubated with human colon carcinoma cell line SW480. We observed that depending on the density of the oligonucleotides on the nanoparticle's surface, cell internalization and antitumoral efficiency vary.

2. EXPERIMENTAL METHODS

2.1. Nanoparticle Synthesis and Coating. Reagents for the γFe_2O_3 nanoparticles (SPIO-NPs) synthesis and analyses were obtained from Sigma-Aldrich (Saint-Quentin Fallavier, France) and were used without further purification. Oligonucleotides dODN 5′-d(CATTTCCCGTAAATCGAAGATTT-ACGGGAAATG) and Mut-dODN 5′-d(CATTTGCCACAA-TCGAAGATTGTGGCAAATG) were purified by reverse-phase HPLC and purchased from Eurogentec (Angers, France).

They contain a 5′ amino modifier C6 group and a fluorescein amidite (FAM) group at the 3′-end. The presence of these two groups at the ends of the dODN contributes to the protection against the exonuclease. Oligonucleotides are self-complementary and can adopt a hairpin structure. Before they were used, the oligonucleotides were heated at 90 °C for 10 min and then allowed to cool slowly to room temperature (below 30 °C).

To immobilize successfully oligonucleotides on the SPIO-NP surface, we first considered the interaction between the iron oxide surface and the large number of phosphate binding groups (33) on the oligonucleotide backbone. Two mechanisms are involved: electrostatic interactions[14] between the positively charged iron oxide surface and negatively charged phosphates and phosphate adsorption bonded through Brønsted acid and/or Lewis coordination leading to a bridge ($-P{=}O{-}Fe$) between two adjacent iron atoms.[15]

The SPIO-NPs were synthesized in a direct micelle system by the reaction of ferrous dodecyl sulfate with dimethylamine according to a procedure described previously.[16] The average size of the bare nanoparticle is 10 nm in diameter (standard deviation σ, 20%) and the isoelectric point (IEP) is about 7 (Figure S1 of Supporting Information). SPIO-NPs were dispersed in 500 μL of water at pH 2 at different concentrations. In these conditions, surface accumulation of hydronium ions leads to a positive surface charge (Figure S1 of Supporting Information).

To study the formation and loading levels of SPIO-NP@dODN complexes, a fixed quantity of FAM-labeled dODN, usually 2 μg, was dissolved in 500 μL of distilled water at pH 7 and mixed with decreasing amounts of SPIO-NPs with stirring during 30 min at 25 °C. In the text, R is defined as the molar ratio between the number of dODN strands and the number of SPIO-NPs: $R = [dODN]/[SPIO-NPs]$. This ratio was varied from 17.5 to 175. To remove uncoated dODN, particles were separated from the supernatant by centrifugation for 30 min at 14 500 rpm. Finally, the nanoparticles were dispersed in water (pH 7).

2.2. Nanocrystal Characterization.
The mean particle size was determined by transmission electron microscopy. The size and the ζ-potential of the nanocomplexes were determined by dynamic laser light scattering on a Nano-ZS (Red Badge) ZEN 3600 device (Malvern Instruments, Malvern, U.K.). Each sample was analyzed at room temperature with diluted ferrofluid ([iron] = 5.10^{-4} mol L^{-1}) at pH 7.4.

2.3. Spectroscopic Characterization.
UV data were obtained using a Kontron Uvikon 942 spectrophotometer (Kontron, Paris, France). The extinction coefficients, expressed in L mol^{-1} cm^{-1}, used for the dODN and the Mut-dODN, were 329 300 and 304 600 at 260 nm, respectively, and 420 for the iron at 480 nm. Fluorescence measurements were performed using an excitation wavelength of 490 nm on a Spex FluoroMax spectrofluorometer equipped with a Hamamatsu 928 photomultiplier (HORIBA Jobin Yvon, Villeneuve D'Ascq, France).

Concerning the Fourier transform infrared (FTIR) spectroscopy, spectra were recorded on a Tensor 27 spectrophotometer (Bruker, Karlsruhe, Germany) at a 1 cm^{-1} resolution, and data treatment was performed using the Opus program. Because of interfering vibrations of H_2O at 1645 cm^{-1}, spectra were recorded in D_2O to study DNA base vibrations (1750–1500 cm^{-1}). Deuteration experiments were performed by drying the samples and dissolving them in a D_2O solution (>99.8% purity, Euriso-Top; CEA, Saclay, France). Solutions were deposited between two ZnSe windows. Samples were studied at an oligonucleotide concentration of 8 mM for the dODN alone and 4 mM for SPIO-NP@dODN.

2.4. DNA Melting Experiments.
Experiments were performed on a Kontron Uvikon 942 spectrophotometer (Kontron, Paris, France). The temperature in the cells was gradually increased from 2 to 80 °C at a rate of 0.16 °C min^{-1} using a circulating bath. All experiments were performed in 10 mM HEPES buffer at pH 7.4. Melting temperatures (T_m) were determined from the first derivative of the melting curves.

2.5. Cell Culture.
The SW480 colon adenocarcinoma cell line was grown in 10% FCS/DMEM (GibcoBRL, Life Technologies, Cergy Pontoise, France) 100 U mL^{-1} penicillin, 10 μg mL^{-1} streptomycin (GibcoBRL), 1 mM sodium pyruvate (GibcoBRL), MEM vitamins 100 (GibcoBRL), and 5 μg mL^{-1} plasmocin (Cayla InvivoGen, Toulouse, France). Cells, at a confluence of 60%, were incubated with nanoparticles for 0.5–24 h on a magnetic plate (OZ Biosciences, Marseilles, France).

2.6. Effect of Magnetic Field: Kinetics of Internalization.
Cells were grown in 6-well plates to a density of 2.5×10^5 cells mL^{-1}. They were incubated on a magnetic plate with SPIO-NP@dODN at an iron concentration of 250 μM. Experiments were performed in duplicate. The uptake of FAM-labeled SPIO-NP@dODN was measured by flow cytometry, gating on a FAM-positive signal using a BD FACS Canto II Flow Cytometer. In parallel, the magnetic properties of the nanoparticles were recorded at room temperature using the MIAtek magnetic sensor developed by Magnisense SE (France). The instrument measures a signal that is proportional to the third derivative of magnetization at a zero magnetic field $((\partial^3 M(H)/\partial H^3))$. Biological samples exhibit virtually no magnetic background; consequently, the MIAtek signal is correlated directly with the amount of magnetic particles.[9] First, a calibration curve is established with the SPIO-NP@dODN stock solution at various concentrations (Figure S2 of Supporting Information). After various times of incubations, the cells were washed three times with buffer, trypsinized, and deposited in tubes for centrifugation. Then the MIAtek signal is measured (Figure S2A,B of Supporting Information). From the previous calibration curve, we deduced the amount of nanoparticles in the tubes containing the cells and thus the percentage of internalized NPs.

2.7. Immunofluorescence and Cell Viability Assays.
Cells were transfected with the SPIO-NP@dODN and incubated on a magnetic plate for 2 h. For immunofluorescence, cells were grown on microscope slides (Lab-Tek, Nunc, U.S.). After 48 h, the cells were washed twice in PBS, fixed in 3.7% formaldehyde in PBS for 15 min, permeabilized in 0.1% Triton X-100 for 15 min, and blocked with 5% FCS and 0.1% Tween in PBS for 1 h. Cells were incubated with the primary antibody (anti-STAT3, dilution 1:100, Cell Signaling) for 1 h and Alexa Fluor 546-labeled secondary antibody (Invitrogen) (1:200) for 90 min. After being counterstained with DAPI, coverslips were mounted onto slides in Vectashield (Vectorlabs, Cliniesciences, Montrouge, France). Fluorescent images were acquired digitally using a Zeiss Axioplan2 Deconvolution microscope (CarlZeiss, Le Pecq, France) and analyzed with Metafer4 (Metasystems, Altlussheim, Germany).

To measure cell death, after 48 h of incubation with SPIO-NP@dODN, cells were resuspended in annexin V-binding buffer, incubated with 5 μL of propidium iodide (BD Pharmingen, Morangis, France), and analyzed by flow cytometry using a BD FACS Canto II Flow Cytometer. Cell

viability was also assessed using the trypan-blue exclusion method.

3. RESULTS AND DISCUSSION

3.1. Hydrodynamic Diameter and ζ-Potential. The colloidal behavior, i.e., hydrodynamic diameter and surface charge, of the nanocomplexes was determined by dynamic laser light scattering in water (pH 7) (Figure 1).
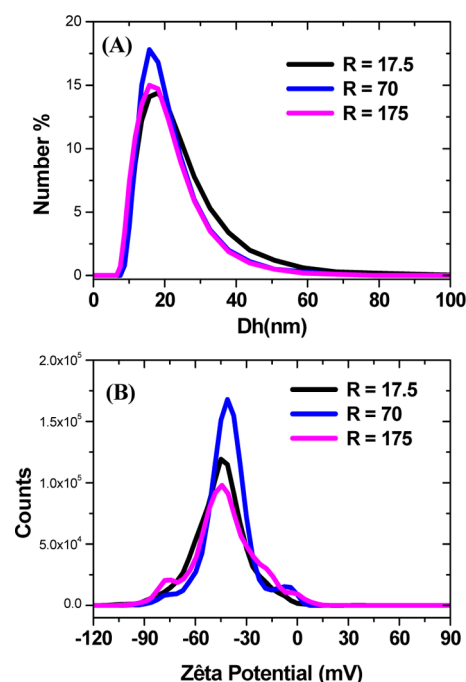

Figure 1. (A) Hydrodynamic diameter (Dh) and (B) ζ-potential distributions measured in water (pH 7) at a $5 \cdot 10^{-4}$ M iron concentration for different values of R.

These measurements are an indication of the stability of the nanocomplexes. The average size, polydispersity index, and ζ-potential are roughly constant whatever the ratio R, which indicates good colloidal stability for each nanocomplex (Table 1). However, we can note that hydrodynamic diameter and

Table 1. Values of Hydrodynamic Diameter (Dh), Polydispersity Index (PdI), and ζ-Potential (Z) Measured in Water (pH 7) at a $5 \cdot 10^{-4}$ M Iron Concentration

R	Dh (nm)	PdI	Z (mV)
17.5	21	0.24	−45
70	19	0.17	−41
175	18	0.17	−42

polydispersity index decrease slightly as oligonucleotides increase. This phenomenon is probably due to a higher stability of the nanocomplexes when the density in dODN increases at the surface of the nanoparticles.

3.2. Number of dODN Strands Per Particle: Spectroscopic Study. A quantitative evaluation of the maximum dODN loading was provided by UV spectroscopy. FAM-labeled dODN is characterized by two absorption peaks at 260 and 490 nm attributed to the dODN and FAM absorption bands, respectively. It can be seen that the FAM-labeled dODN presents no absorption at 350 nm (Figure S3A of Supporting

Information). The absorption spectra of SPIO-NP@dODN obtained at various R are presented in Figure 2A.

The nanocomplexes were prepared with a fixed concentration of oligonucleotide and decreasing amounts of nanoparticles as R increased. The iron oxide absorption at 350 nm and the contributions of the FAM-labeled dODN, i.e., two additional shoulders at 260 and 490 nm, can be observed clearly. To take into account the absorption of SPIO-NPs at 260 nm, in addition to the absorption of dODN, Figure 2B shows the evolution of the UV absorbance ratio A_{260}/A_{350} versus R. The signal rose linearly with the increase of the molar ratio R up to 70 dODN strands per particle, whereupon it reached a plateau. This indicates an increase of the number of dODN strands on the SPIO-NPs surfaces with ratio R and a saturation corresponding to an average of 70 ODN per nanoparticle. Analysis of the UV spectra of the supernatants (Figure S4 of Supporting Information) revealed that below $R =$ 70, almost all the dODN strands have been adsorbed onto the SPIO-NPs surfaces, whereas beyond this ratio, an excess of DNA is not taken up.

The emission of fluorophores is known to be very sensitive to the surroundings. Quenching occurs because of the interaction of fluorophores with the metal oxide particle surface (Scheme 1(1)), intermolecular quenching onto the nanoparticle (Scheme 1(2)), and/or between nanoparticles (Scheme 1(3)).

The emission band characteristic of the FAM-labeled dODN is localized at 514 nm (Figure S3B of Supporting Information). Figure 3 shows the influence of nanoparticle concentration on fluorescence intensity corresponding to a ratio of $R = 17.5$. Interparticle quenching is observed for [iron] > 250 μM.

Fluorescence experiments were performed at fixed nanoparticle numbers and diluted concentration: [iron] = 64 μM. In this condition, the interparticle quenching is expected to be negligible. The emission spectra of SPIO-NP@dODN obtained at various R are presented in Figure 4A. The evolution of fluorescence intensity at 514 nm versus R is also reported (Figure 4B).

In accordance with the absorption study (Figure 2B), an increase of fluorescence intensity with ratio R is observed in Figure 4B, reaching a plateau at about 70 dODN per nanoparticle. By taking into account that the average number of oligonucleotides increases with R up to 70, the evolution of fluorescence quenching with the amount of dODN per nanoparticle can be deduced from the calibration curve of the dODN alone (Figure S5 of Supporting Information). As shown in Table 2, it can be observed that maximum quenching is when $R = 17.5$ (88%), and it decreases as the dODN amount increases, reaching a plateau for high DNA densities.

The interpretation of data for $R \leq 70$ must consider two opposing effects. Because of the increase of the FAM-dODN loading with R values, an enlargement of the intermolecular quenching is expected. An opposite effect could be related to a change of the FAM−nanoparticle surface distance. Increasing the distance between the fluorophore and the nanoparticle surface should lead to a decrease of fluorescence quenching due to weaker interactions between the two entities.[17] In the present study, the oligonucleotide is self-complementary and can adopt a hairpin structure. The FAM is localized at the 3′-end of the dODN. It can be suggested that for low dODN loading, the dODN in hairpin structure is fully condensed on the nanoparticle surface (Scheme 2A).
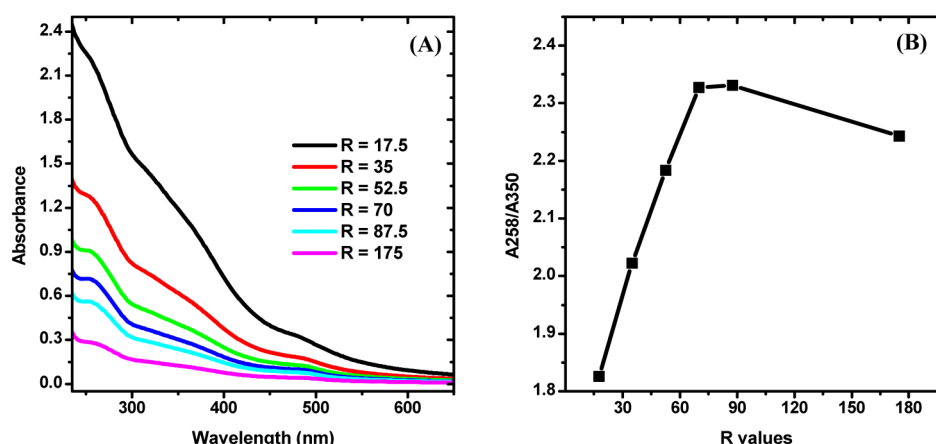
Figure 2. UV spectra (A) and evolution of the ratio A_{260}/A_{350} (B) of the nanocomplexes obtained for different values of R in water (pH 7).

Scheme 1. Illustration of Some Processes of Fluorescence Quenching
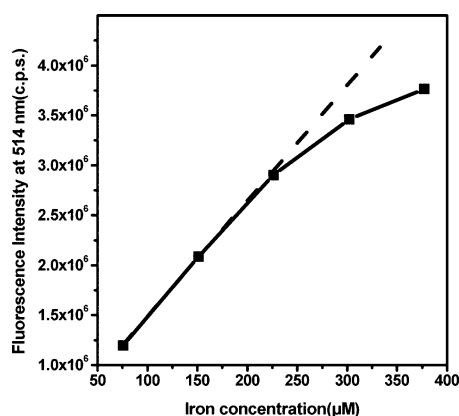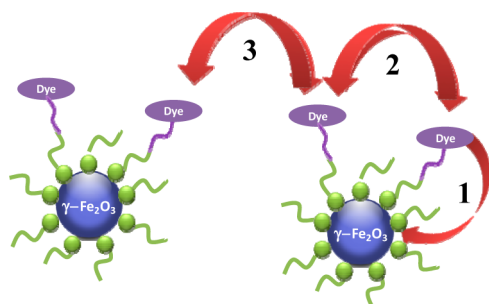

Figure 3. Evolution of the fluorescence intensity versus the iron concentration for the ratio $R = 17.5$ (solid line) and guideline for linear evolution (dotted line).

Increasing the ratio R induces a highly ordered surface packing assembly of dODN perpendicular to the nanoparticle surface, keeping the hairpin structure or a random-coil state (Scheme 2B,C). With this assumption, the distance between the FAM group and the nanoparticle surface increases with ratio R, reducing the quenching effect. Similar phenomena were observed by considering the structure adopted by single-stranded DNA (ssDNA) on the surface of gold. For example, it is generally observed that when the grafting density is low, DNA immobilizes in a flat conformation through nonspecific adsorption.[18] At high grafting densities, repulsive interactions force the DNA strands to extend away from the surface and densely packed DNA strand films are observed.[19] Changes in

fluorescence intensity have been also reported using fluorophore-labeled DNA with a gold surface. Depending on the distance between the fluorophore and the gold surface, complete quenching to extensive enhancement has been reported.[20] A recent work by Opdahl and co-workers describes drastic changes observed upon the hairpin opening on a flat gold surface[21] using TAMRA as a fluorescence probe. In this paper, complete quenching is reported when the hairpin axis is parallel to the gold surface, while fluorescence increases significantly when the fluorophore is moving away from the surface because of hairpin opening induced by stringency modification or competition with a neighboring DNA strand.

By considering all these data, we attribute the changes observed in the quenching ratio (Table 2) to a modification in the orientation of the dODN, which could be oriented either horizontally or vertically to the surface as the density varies. At high ratio, the fully condensed dODN structure on the iron oxide surface, in hairpin conformation or random-coil state, could not be discriminated at this step of the study.

3.3. Orientation and Surface Density of Oligonucleotide: Geometrical Model. The diameter of the double helix in a classical DNA is between 2 and 2.6 nm, and the pitch, which is the width of one helix turn corresponding to ten base pairs, is 3.4 nm.[22,23] The hairpin structure of the dODN used in this work, approximately 15 base pairs, could be schematized as a cylinder with a radius of around 1 nm and a height of 5.1 nm (Scheme 2). The simplistic calculation, by considering the surface of the nanoparticle (314 nm^2) and the base surface of the cylinder (between 3.14 and 5.31 nm^2), shows that it is possible to coat roughly a maximum of 24−31 dODN strands when they are condensed horizontally on the nanoparticle surface (Scheme 2A), 60−100 when they are adsorbed perpendicularly to the surface in a hairpin structure (Scheme 2B), and 240−400 strands when they are in a random-coil state (Scheme 2C). In this simplistic model, several assumptions are made. The nanoparticles are assumed to be perfect spheres 10 nm in diameter, and we do not take into account size polydispersity, steric hindrance between the DNA strands, and the electrostatic repulsion between the phosphate groups. These two latter parameters should reduce the maximum number of dODN per nanoparticle in the three configurations. Nevertheless, this model shows that the experimental determination of 70 DNA strands as a maximum number per nanoparticle is not unrealistic. Furthermore, by considering the hydrodynamic diameter variation with ratio R (see 3.1
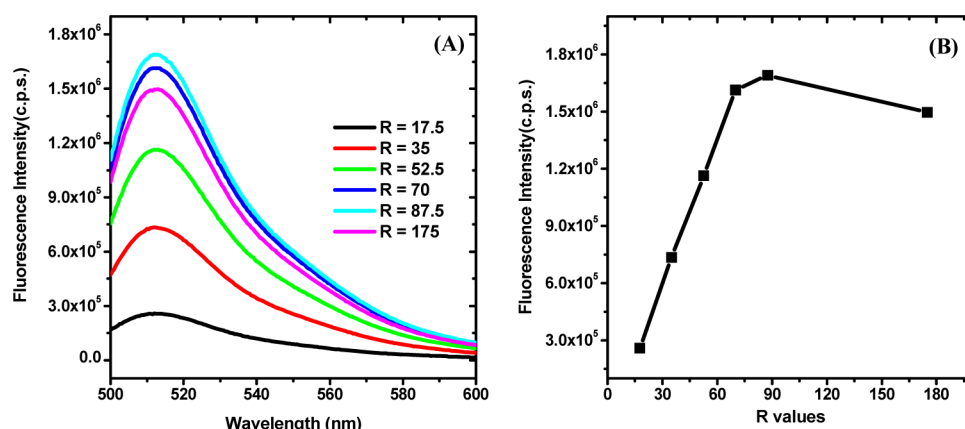
Figure 4. Fluorescence spectra (A) and evolution of the fluorescence intensity at 514 nm (B) of the nanocomplexes obtained for different values of R in water (pH 7).

Table 2. Evolution of Fluorescence Quenching with R Value

R	quenching (%)
17.5	88
35	78
52.5	73
70	71
87.5	70
175	72

Scheme 2. Schematic Representation of dODN Organization on the Nanoparticle Surface: dODN Fully Condensed on Nanoparticle in Hairpin Structure (A), Perpendicular to the Nanoparticle Surface in Hairpin Structure (B), and in Random-Coil State (C)
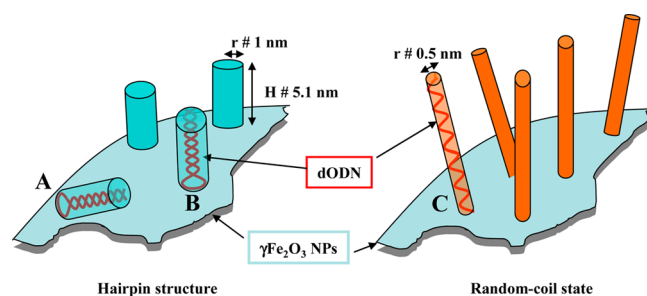
Hydrodynamic Diameter and ζ-Potential), it seems in the first approximation that the dODN retains a hairpin structure on the nanoparticle surface. Similar results were reported previously for thiolated oligonucleotides loading on gold nanoparticles.[24] The maximum surface density of oligonucleotides for our nanoparticles, calculated by dividing the number of oligonucleotides per particle by the calculated surface area (in centimeters squared), is around 2×10^{13} oligonucleotides cm^{-2}, i.e., 0.22 strands nm^{-2}. This result is similar to the surface coverage proposed by Chad Mirkin and co-workers for 10 nm diameter gold nanoparticles functionalized with a ssDNA.[24] Similar densities, $1-6 \times 10^{13}$ molecules cm^{-2}, depending upon the buffer, were obtained by Petrovykh and Whitman with ssDNA immobilized on a flat gold surface.[18]

The effective DNA footprint (i.e., the average area of one oligonucleotide per nanoparticle surface) for our nanocomplex is 4.5 nm^2. From this value, which is close to that found by Mirkin et al., we can estimate a distance of 12.5 Å between neighboring double strand (ds) DNA onto one particle.[24] This

distance is greater than the intrastrand phosphate−phosphate distance (around 7 Å) and is greater than the minimum van der Waals contact distance between two oxygen or phosphor atoms (around 3−4 Å). This could justify the high density of dsDNA on the iron oxide nanoparticle surface in comparison with results obtained with condensed ssDNA on the gold nanoparticle surface. In this latter case, such ssDNA assemblies require high salt concentration because the electrostatic repulsion of the initially adsorbed DNA otherwise repels any additional ssDNA that would attempt to adsorb.

3.4. dODN Structure on the Nanoparticle. FTIR experiments were carried out to analyze the characteristics of the oligonucleotide on the nanoparticles. Infrared spectroscopy is a method of choice for studying the structure and interaction of nucleic acids, yielding information on base pairing, the nature of the helix, and sugar pucker or vibration along the sugar−phosphate chain.[9,25−28] To study DNA base vibrations (1750−1500 cm^{-1}) and symmetric PO_2^- stretching vibrations (1150−1000 cm^{-1}), spectra were recorded in D_2O. The spectra of the free oligonucleotide in the double-stranded structure (25 °C) and in the random coil state (after heating at 95 °C) are presented in Figure 5 as spectrum a and b, respectively.

The main differences are observed in the region of the base vibrations where the characteristic bands of the Watson−Crick base pairing are present at 25 °C, whereas they disappear at 95 °C.[9,25−28] After complexation on the nanoparticle surface, the in-plane base vibrations (Figure 5, left panel, spectra c and d) and the sugar−phosphate vibrations of DNA (Figure 5, right panel, spectra c and d), correspond mainly to an oligonucleotide in a double-stranded structure (Figure 5, spectrum a). Nevertheless, for the nanocomplex obtained with a molar ratio of 17.5, some modifications are observed in the 1500−1750 cm^{-1} domain (Figure 5, left panel, spectrum e). In this region, the vibrations of the bases are extremely sensitive not only to base pairing interactions but also to base stacking.[9,25−28] Considering that for the ratio $R = 17.5$ the dODN is condensed horizontally on the nanoparticle surface, the base vibrations modification could be due to several end base pairs opening in order to interact with the NP surface. Such modifications have been reported in the case of double-stranded DNA adsorbed horizontally on a graphene surface.[29] A slight modification of the spectra is also observed in the region containing the sugar−phosphate and sugar vibrations of DNA (Figure 5, right panel, spectrum e). The broadening of the band in the region between 1150 and 1000 cm^{-1} reflects the interactions of some
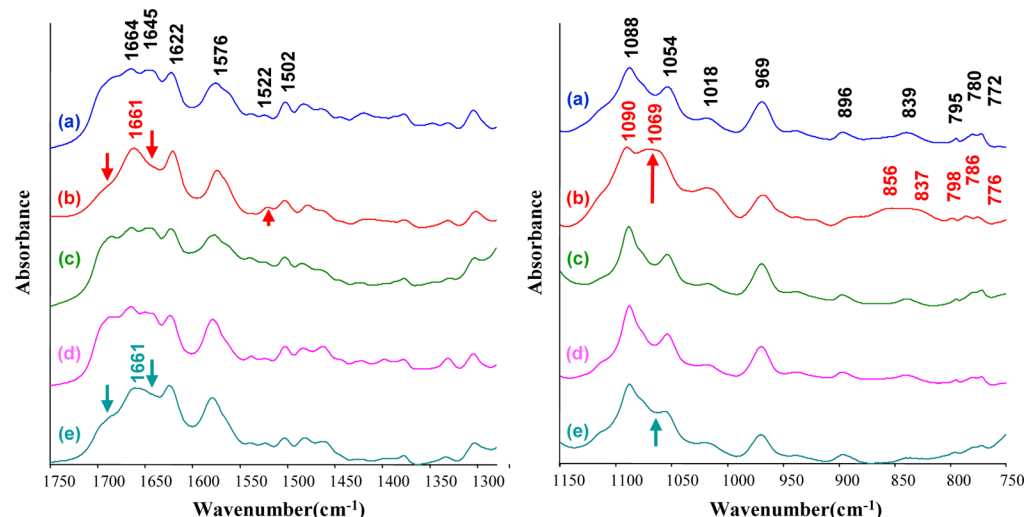
Figure 5. FTIR evidence of the dODN structure on the NPs surface. FTIR spectra recorded in D_2O in the region of the in-plane base vibrations (left panel) and the sugar−phosphate vibrations (right panel). Spectrum of the free dODN at 25 °C (a) and 95 °C (b). Spectrum of the SPIO-NP@dODN with a molar ratio of 175 (c), 70 (d), and 17.5 (e).

phosphates with the nanoparticle surface.[14,30] Slight modifications in the in-plane base vibrations and sugar−phosphate regions suggest that the interaction between the oligonucleotide and the particle could take place through few phosphate groups, leading to perturbations in the base stacking.[9,25−28]

UV thermal denaturation is a convenient method for the evaluation of DNA base pairing, and it can provide information on the thermal stability of the oligonucleotides structures.[31−33] By regarding the potential structural modifications of the dODN upon its surface complexation, UV melting experiments have been performed on the free oligonucleotide and SPIO-NP@dODN nanoparticles obtained at various molar ratios R (Figure 6).
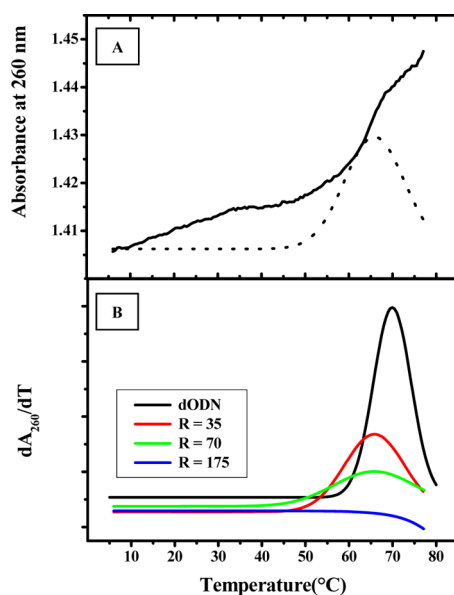

Figure 6. Evolution of the dODN structure depending on R, the molar ratio between dODN and nanoparticle. (A) UV melting curve of SPIO-NP@dODN with an R value of 35 (solid line) and the related derivative (dotted line). (B) Gaussian fit of the first derivative of the UV melting curves for the free dODN (black), SPIO-NP@dODN with an R value of 35 (red), 70 (green), and 175 (blue).

The T_m of the free oligonucleotide was found independent of the DNA concentration, thereby confirming an intramolecular hairpin structure.[9] The dODN and SPIO-NP@dODN denaturation curves differ not only from their T_m value but also from their overall shapes. Indeed, the melting curves of the adsorbed DNA show reduced cooperativity compared to that of the "free" oligonucleotide, as confirmed by the broadening shape of the first derivatives (Figure 6B). DNA duplex formation or denaturation is known to be a highly cooperative process determined by the stacking interactions between neighboring base pairs formed sequentially and also by the conformational properties of the sugar−phosphate backbone.[33] UV melting experiments show (Figure 6A), under our experimental conditions, that for a low molar ratio ($R = 35$ in this case), the hairpin structure is at least partially conserved, even if it is slightly destabilized by the interactions between the phosphate groups and the maghemite (Figure 6B). On the other hand, when the molar ratio increased, the sigmoidal shape disappeared progressively. This observation could be explained by considering at least two phenomena. First, when surface density (ratio R) increases, the denaturation of the hairpin dODN to a random-coil state occurs naturally. Alternatively, the immobilized dODN strands, still in the hairpin structure, are close to each other, thereby reducing the special freedom that is necessary for a cooperative denaturation enhancement. By considering the FTIR data, weak variations of the hydrodynamic diameter, and the surface charge of the nanocomplexes, the second assumption seems more accurate.

This result is in apparent disagreement with previous work involving oligonucleotide gold nanoparticle conjugates.[34,35] These studies concern intermolecular duplexes with DNA-linked nanoparticle structures. In our case, the duplex which is intramolecular (hairpin structure) is not shared between two particles and the DNA strand is attached directly close to the surface of an iron oxide nanoparticle without linker. Differences in melting cooperativity could be explained by the physical nature of the two systems. Indeed, the dramatic broadening of the thermal denaturation duplex melting curve for surface-tethered DNA has already been reported by Pettitt and co-workers.[36,37] Their model of the Coulomb effects for surface-

bound DNA can explain the thermal denaturation curve broadening as the probe surface density increases.

3.5. Nanocomplex Stability in Serum and Cell Internalization As a Function of Time. The stability of the electrostatic nanocomplexes formed between the dODN and the nanoparticles was characterized using fluorescence spectroscopy, after dilution in 10% serum. The fluorescence measurements were performed for nanocomplexes corresponding to ratios $R = 17.5$ and $R = 70$ (corresponding to surface saturation) and for dODN alone with an oligonucleotide concentration of 25 nM. The fluorescence intensity has been displayed as a function of time in order to estimate the dODN release profile (Figure 7).
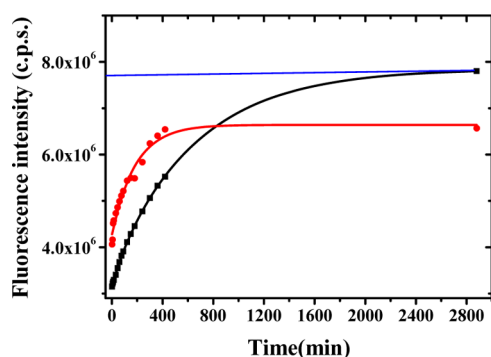

Figure 7. Fluorescence intensity of dODN nanocomplexes for $R = 17.5$ (black), $R = 70$ (red), and that of free dODN (blue) in the presence of 10% serum.

Indeed, for both dODN nanocomplexes ($R = 17.5$ and $R = 70$), the fluorescence intensity increases as a function of time (Figure 7, black and red curves), whereas the free dODN

fluorescence is constant (Figure 7, blue line). This increase of fluorescence suggests dODN release. Assuming that all dODN strands are released from the nanoparticle surface after 48 h of incubation, we deduced that in the presence of 10% serum, half of the oligonucleotide is released in the solution after 408 and 128 min for $R = 17.5$ and $R = 70$, respectively. The difference in the half-time release between the two nanocomplexes has to be related to the oligonucleotide packing because for $R = 17.5$, the number of phosphate groups in interaction with the surface is potentially greater than that for $R = 70$, as confirmed by the FTIR spectroscopy (see 3.4 dODN Structure on the Nanoparticle). Nevertheless, for both nanocomplexes, these half-lives are comparable with those obtained with other systems.[38]

To monitor nanoparticle cell internalization and to confirm that our nanocomplexes should deliver the dODN before their release, flow cytometry and magnetic measurements were performed. We have demonstrated previously the high efficiency of the magneto internalization of nanoparticles with other nanosystems.[9,39,40] Human colon carcinoma SW480 cells were grown in 24-well plates and were incubated in the presence of a magnet for different times, from 30 min to 24 h, in duplicate, with nanocomplexes corresponding to ratios of $R = 17.5$ and $R = 70$ at [iron] = 250 μM.

The uptake of FAM-labeled SPIO-NP@dODN was measured by flow cytometry and magnetic quantification as a function of time (Figure 8).

Both experiments complement each other because the flow cytometry measures the percentage of fluorescent cells and the MIAtek reader (Magnetic ImmunoAssays technology) is used to quantify the SPIO-NPs internalized in the cells.[9,41−43] The detection threshold is units of nanograms of NPs. The quantity of iron internalized by the cells was deduced from a calibration curve (Figure S2 of Supporting Information).
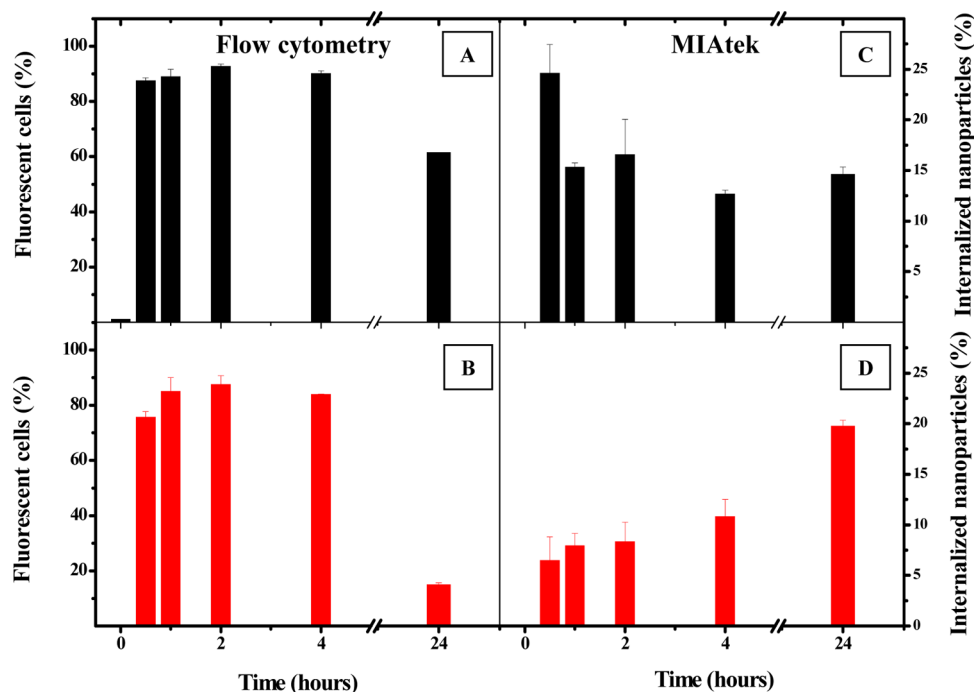

Figure 8. Quantification of the internalization of nanocomplexes by SW480 colon carcinoma cells. Percentage of transfected cells versus the time of incubation in the culture media for $R = 17.5$ (A) and $R = 70$ (B) nanocomplexes measured by flow cytometry. Percentage of internalized nanoparticles versus the time of incubation for $R = 17.5$ (C) and $R = 70$ (D) nanocomplexes measured by magnetic measurements.
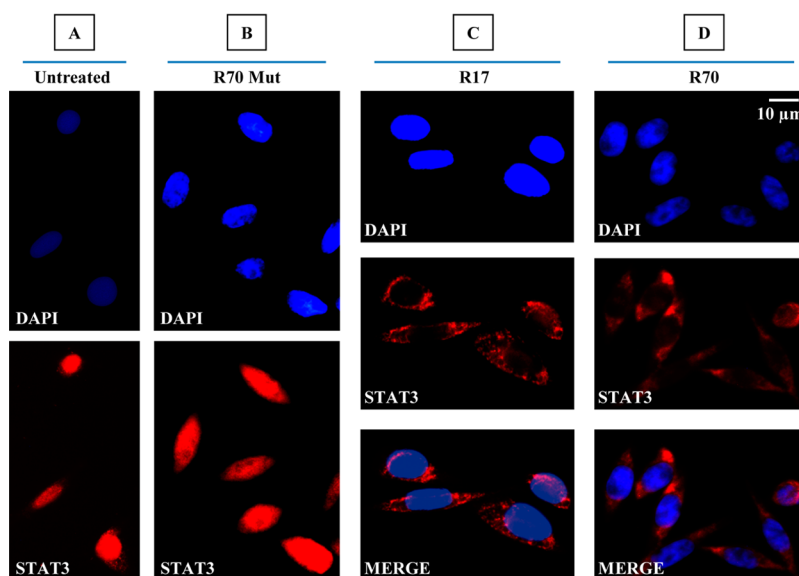
Figure 9. Inhibition of STAT3 nuclear localization by SPIO-NP@dODN in SW480 colon carcinoma cells. (A) Nuclear localization of STAT3 in untreated SW480 cells. (B) Nuclear localization of STAT3 in SW480 cells treated with SPIO-NP@Mut-dODN. (C and D) Cytoplasmic localization of STAT3 in SW480 cells treated with SPIO-NP@dODN $R = 17.5$ (C) and $R = 70$ (D). (1) DAPI was used to stain the nuclei (blue). (2) Cells were fixed and labeled with anti-STAT3 antibody (red). (3) Merged fluorescence images.

The magnetic quantification was expressed as relative units (percent). The mean values found here in percent (Figure 8C,D), associated with their standard deviation, were obtained by dividing the number of internalized nanoparticles by the number of incubated nanoparticles. As can be seen in Figure 8C,D, the amount of SPIO-NPs loaded in the cells differs with the amount of dODN per nanoparticles. For $R = 17$, the maximum of internalized nanoparticles (25%) is obtained after only 30 min of incubation (Figure 8C). For $R = 70$, the intracellular iron concentration increases with time and it is not saturated even after 24 h of incubation (20%) (Figure 8D). It can also be observed that for $R = 70$, nanocomplexes are internalized more slowly than for $R = 17$: 8% and 25% of internalization, respectively, after 30-min incubation. This difference in kinetic behavior of the two nanocomplexes has to be related to the oligonucleotide packing.

In parallel with the magnetic experiments, the cytometry study (Figure 8A,B) shows that the maximum number of fluorescent cells is obtained after only 2 h of incubation for both nanocomplex ratios. At 2 h, the transfection efficiency is slightly higher for $R = 17$ (93%) than for $R = 70$ (85%). It is also noticeable that for both samples, the number of fluorescent cells detected by flow cytometry decreases after 24 h of incubation, whereas it was observed with the MIAtek signal that the amount of nanoparticles saturates for $R = 17$ and increases for $R = 70$ at 24 h. This suggests two hypotheses: (i) either degradation of the fluorophore or (ii) fluorescence quenching occurs because of nanoparticle aggregation after a long duration under an applied magnetic field because of nanoparticle accumulation within cells.

Hence, from their half-time release (from 120 to 400 min) and their internalization time (about 60 min), the as-synthesized nanocomplexes should deliver their dODN loading into the cells. Moreover, it can be expected that the kinetics of internalization and the biological activity of the nanocomplexes will be dependent on the oligonucleotide packing.

3.6. Biological Assays. The signal transducer and activator of transcription STAT3 is a transcription factor that plays a key role in normal cell growth and is activated constitutively in about 70% of solid and hematological cancers. STAT3 is activated by a tyrosine phosphorylation in the cytoplasm and consecutively forms a dimer. The dimer enters the nucleus via an interaction with importins and thus binds target genes. In previous work, is has been shown that this dODN was biologically active and prevented the nuclear translocation of STAT3, leading to an abnormal cytoplasmic concentration of STAT3 dimers.[12] Inhibition of STAT3 results in the death of tumor cells, which indicates that it is a valuable target for anticancer strategies.

To study the interaction of nanocomplexes with STAT3, immunofluorescence microscopy was used to show the subcellular localization of STAT3, i.e., cytoplasmic or nuclear localization, in SW480 colon carcinoma cells. Bare γFe_2O_3 nanoparticles could not be tested as control NPs because of their precipitation in the culture medium (IEP $\neq$ 7, Figure S1 of Supporting Information). Consequently, for control measurements, the nanoparticles were surface-functionalized with a nonspecific STAT3 ODN (Mut-dODN) using the same procedure and ratio as that for the FAM-dODN. Cells were incubated for 48 h with nanocomplexes at the molar ratio $R = 17$ or 70. The magnetic field was applied during the first two hours.

As expected, in the control cells, untreated cells, and cells treated with the Mut-dODN nanoparticles, STAT3 is localized mostly in the nuclei (Figure 9A,B).

On the other hand, when the cells were incubated in the presence of SPIO-NP@dODN, STAT3 was essentially cytoplasmic whatever the molar ratio (Figure 9C,D). The cytoplasmic localization of STAT3 after treatment confirms that the nanoparticles can prevent the nuclear translocation of STAT3 and thus the internalization of the SPIO-NP@dODN into the SW480 cell line.

To examine the transfection efficiency of nanocomplexes, cell death was evaluated at 48 h either by flow cytometry for propidium iodide incorporation and annexin V labeling or with a Malassez counting chamber by measuring trypan blue uptake.

1542

dx.doi.org/10.1021/jp410899a | J. Phys. Chem. B 2014, 118, 1535−1544

The results obtained using these two methods were similar. Figure 10 reports the percentage of dead cells measured by the trypan blue exclusion method. Data related to flow cytometry are presented in Figure S6 of Supporting Information.
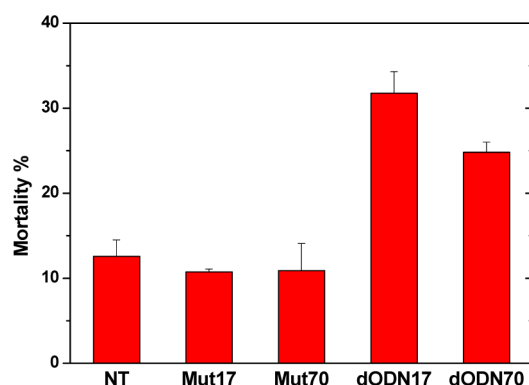

Figure 10. Percentage of cell mortality measured by the trypan blue exclusion method. Cells were either nontreated (NT), or treated with SPIO-NP@dODN at a ratio of 17.5 (dODN17) or 70 (dODN70) and with SPIO-NP@Mut-dODN at a ratio of 17.5 (Mut17) or 70 (Mut70).

At the molar ratio of 17.5 (Figure 10, dODN17), the percentage of dead cells was 32%. This result is similar to that obtained with other vectors.[12] However, the percentage of dead cells obtained with a molar ratio of 70 was the smallest (25%) (Figure 10, dODN70) for the same amount of internalized dODN; around 2 μg of dODN for 200 000 cells (MIAtek measurement, data not shown). Possible explanations for this phenomenon could be the steric hindrance of the dODN onto the particles for $R = 70$, which could reduce the approach of STAT3 compared with the ratio $R = 17.5$. Cell death can be attributed to the specificity of the SPIO-NP@dODN because the mortality of the SW480 cells incubated with the SPIO-NP@Mut-dODN (Figure 10, Mut17 and Mut70) is quite similar to that observed for the nontreated cells (Figure 10, NT): 11% and 13%, respectively. The first results presented here show that the SPIO-NP@dODN can induce the death of SW480 colon carcinoma cells by inhibiting the nuclear translocation of STAT3 and that their action seems to be dependent on the orientation adopted by the oligonucleotide on the nanoparticle surface. Further improvements to optimize the induction of the apoptosis could be the modulations of the dODN loading, size of the nanoparticles, iron concentration, or time of incubation

4. CONCLUSION

In this study, we report a simple process for the direct and one-step complexation of a labeled decoy oligonucleotide (dODN) with iron oxide nanoparticles to obtain bioactive nanoparticles. Internalized SPIO-NP@dODN specifically target the signal transducer and activator of transcription STAT3 into the cytoplasm, prevent the nucleus translocation of STAT3, and induce the death of SW480 colon carcinoma cells. This method allows control of the DNA loading. Up to 70 DNA strands are adsorbed onto the 10 nm particle surface. At low molar ratios, the dODN is stretched out onto the nanoparticle surface. Increasing the ratio R induces a highly ordered surface packing assembly of dODN while retaining their hairpin structure. Our results demonstrate that the kinetics of internalization and the

biological activity of the decoy SPIO-NP@dODN into the SW480 cells are dependent on the density of the oligonucleotide on the nanoparticle surface. The more dODN that are grafted, the more their internalization rate is slowed and the more the inhibition of STAT3 is weakened. This simple process, by decreasing synthesis time, intermediates, and derivatives, makes this superparamagnetic DNA carrier particularly attractive for further applications in genetic regulation, intracellular detection, or therapeutics.

■ ASSOCIATED CONTENT

Ⓢ Supporting Information

Hydrodynamic diameter and ζ-potential values of uncoated naoparticles as a function of pH (Figure S1), calibration curves obtained by MIAtek for the SPIO-NP@dODN (Figure S2), UV and fluorescence spectra of the dODN (Figure S3), UV spectra of the supernatants after complexation of the dODN onto the SPIO-NPs surface (Figure S4), calibration curve of the dODN obtained by fluorescence spectroscopy (Figure S5), and cell mortality measured by flow cytometry using propidium iodide incorporation and annexin V labeling (Figure S6). This material is available free of charge via the Internet at http://pubs.acs.org.

■ AUTHOR INFORMATION

Corresponding Author

*Phone: 33 1 48 38 77 07. Fax: 33 1 48 38 85 28. E-mail: laurence.motte@univ-paris13.fr.

Notes

The authors declare no competing financial interest.

■ REFERENCES

(1) Morishita, R.; Gibbons, G. H.; Horiuchi, M.; Ellison, K. E.; Nakajima, M.; Zhang, L.; Kaneda, Y.; Ogihara, T.; Dzau, V. J. A Gene Therapy Strategy Using a Transcription Factor Decoy of the E2F Binding Site Inhibits Smooth Muscle Proliferation in vivo. *Proc. Natl. Acad. Sci. U.S.A.* **1995**, *92*, 5855−5859.

(2) Barton, B. E.; Murphy, T. F.; Shu, P.; Huang, H. F.; Meyenhofer, M.; Barton, A. Novel Single-Stranded Oligonucleotides that Inhibit Signal Transducer and Activator of Transcription 3 Induce Apoptosis in vitro and in vivo in Prostate Cancer Cell Lines. *Mol. Cancer Ther.* **2004**, *3*, 1183−1191.

(3) Mislick, K. A.; Baldeschwieler, J. D. Evidence for the Role of Proteoglycans in Cation-Mediated Gene Transfer. *Proc. Natl. Acad. Sci. U.S.A.* **1996**, *93*, 12349−12354.

(4) Mounkes, L. C.; Zhong, W.; Cipres-Palacin, G.; Heath, T. D.; Debs, R. J. Proteoglycans Mediate Cationic Liposome-DNA Complex-Based Gene Delivery in vitro and in vivo. *J. Biol. Chem.* **1998**, *273*, 26164−26170.

(5) De Fougerolles, A.; Vornlocher, H. P.; Maraganore, J.; Lieberman, J. Interfering with Disease: A Progress Report on siRNA-Based Therapeutics. *Nat. Rev. Drug Discovery* **2007**, *6*, 443−453.

(6) Bumcrot, D.; Manoharan, M.; Koteliansky, V.; Sah, D. W. RNAi Therapeutics: A Potential New Class of Pharmaceutical Drugs. *Nat. Chem. Biol.* **2006**, *2*, 711−719.

(7) Kleinman, M. E.; Yamada, K.; Takeda, A.; Chandrasekaran, V.; Nozaki, M.; Baffi, J. Z.; Albuquerque, R. J.; Yamasaki, S.; Itaya, M.; Pan, Y.; et al. Sequence- and Target-Independent Angiogenesis Suppression by siRNA via TLR3. *Nature* **2008**, *452*, 591−597.

(8) Verma, I. M.; Somia, N. Gene Therapy - Promises, Problems and Prospects. *Nature* **1997**, *389*, 239−242.

(9) Geinguenaud, F.; Souissi, I.; Fagard, R.; Motte, L.; Lalatonne, Y. Electrostatic Assembly of a DNA Superparamagnetic Nano-Tool for Simultaneous Intracellular and in situ Monitoring. *Nanomedicine* **2012**, *8*, 1106−1115.

(10) Al Zaid Siddiquee, K.; Turkson, J. STAT3 as a Target for Inducing Apoptosis in Solid and Hematological Tumors. *Cell Res.* **2008**, *18*, 254−267.

(11) Fletcher, S.; Turkson, J.; Gunning, P. T. Molecular Approaches Towards the Inhibition of the Signal Transducer and Activator of Transcription 3 (Stat3) Protein. *Chem. Med. Chem.* **2008**, *3*, 1159−1168.

(12) Souissi, I.; Najjar, I.; Ah-Koon, L.; Schischmanoff, P. O.; Lesage, D.; Le Coquil, S.; Roger, C.; Dusanter-Dourt, I.; Varin-Blank, N.; Cao, A.; et al. A STAT3-Decoy Oligonucleotide Induces Cell Death in a Human Colorectal Carcinoma Cell Line by Blocking Nuclear Transfer of STAT3 and STAT3-Bound NF-kB. *BMC Cell Biol.* **2011**, *12*, 14.

(13) Sen, M.; Thomas, S. M.; Kim, S.; Yeh, J. I.; Ferris, R. L.; Johnson, J. T.; Duwuri, U.; Lee, J.; Sahu, N.; Joyce, S.; et al. First-in-Human Trial of a STAT3 Decoy Oligonucleotide in Head and Neck Tumors: Implications for Cancer Therapy. *Cancer Discovery* **2012**, *8*, 694−705.

(14) Wang, J.; Gao, L. Surface Properties of Polymer Adsorbed Zirconia Nanoparticles. *Nanostruct. Mater.* **1999**, *11*, 451−457.

(15) Mäkie, P.; Westin, G.; Persson, P.; Österlund, L. Adsorption of Trimethyl Phosphate on Maghemite, Hematite, and Goethite Nanoparticles. *J. Phys. Chem. A* **2011**, *115*, 8948−8959.

(16) Lalatonne, Y.; Paris, C.; Serfaty, J.-M.; Weinmann, P.; Lecouvey, M.; Motte, L. Bis-Phosphonates−Ultra Small Superparamagnetic Iron Oxide Nanoparticles: A Platform Towards Diagnosis and Therapy. *Chem. Commun.* **2008**, *22*, 2553−2555.

(17) Corr, S. A.; Rakovich, Y. P.; Gun'ko, Y. K. Multifunctional Magnetic-Fluorescent Nanocomposites for Biomedical Applications. *Nanoscale Res. Lett.* **2008**, *3*, 87−104.

(18) Petrovykh, D. Y.; Kimura-Suda, H.; Whitman, L. J.; Tarlov, M. J. Quantitative Analysis and Characterization of DNA Immobilized on Gold. *J. Am. Chem. Soc.* **2003**, *125*, 5219−5226.

(19) Pei, H.; Zuo, X.; Pan, D.; Shi, J.; Huang, Q.; Fan, C. Scaffolded Biosensors with Designed DNA Nanostructures. *NPG Asia Mater.* **2013**, DOI: 10.1038/am.2013.22.

(20) Kang, J.; Wang, J.; Jasinski, J. B.; Achilefu, S. Fluorescence Manipulation by Gold Nanoparticles: From Complete Quenching to Extensive Enhancement. *J. Nanobiotechnol.* **2011**, *9*, 16.

(21) Schreiner, S. M.; Hatch, A. L.; Shudy, D. F.; Howard, D. R.; Howell, C.; Zhao, J.; Koelsch, P.; Zharnikov, M.; Petrovykh, D. Y.; Opdahl, A. Impact of DNA-Surface Interactions on the Stability of DNA Hybrids. *Anal. Chem.* **2011**, *83*, 4288−4295.

(22) Watson, J. D.; Crick, F. H. C. A Structure for Deoxyribose Nucleic Acid. *Nature* **1953**, *171*, 737−738.

(23) Mandelkern, M.; Elias, J. G.; Eden, D.; Crothers, D. M. The Dimensions of DNA in Solution. *J. Mol. Biol.* **1981**, *152*, 153−161.

(24) Hill, H. D.; Millstone, J. E.; Banholzer, M. J.; Mirkin, C. A. The Role Radius of Curvature Plays in Thiolated Oligonucleotide Loading on Gold Nanoparticles. *ACS Nano* **2009**, *3*, 418−424.

(25) Liquier, J.; Taillandier, E. Infrared Spectroscopy of Nucleic Acids. In *Infrared Spectroscopy of Biomolecules*; Mantsch, H. H., Chapman, D., Eds.; Wiley-Liss: New York, 1996; pp 131−158.

(26) Banyay, M.; Sarkar, M.; Gräslund, A. A Library of IR Bands of Nucleic Acids in Solution. *Biophys. Chem.* **2003**, *104*, 477−488.

(27) Tsuboi, M. Application of Infrared Spectroscopy to Structure Studies of Nucleic Acids. In *Applied Spectroscopy Reviews*; Brame, E. G. J., Ed.; Dekker: New York, 1969; pp 45−90.

(28) Geinguenaud, F.; Calandrini, V.; Teixeira, J.; Mayer, C.; Liquier, J.; Lavelle, C.; Arluison, V. Conformational Transition of DNA Bound to Hfq Probed by Infrared Spectroscopy. *Phys. Chem. Chem. Phys.* **2011**, *13*, 1222−1229.

(29) Liu, J. Adsorption of DNA onto Gold Nanoparticles and Graphene Oxide: Surface Science and Applications. *Phys. Chem. Chem. Phys.* **2012**, *14*, 10485−10496.

(30) Daou, T. J.; Begin-Colin, S.; Grenèche, J. M.; Thomas, F.; Derory, A.; Bernhardt, P.; Legaré, P.; Pourroy, G. Phosphate Adsorption Properties of Magnetite-Based Nanoparticles. *Chem. Mater.* **2007**, *19*, 4494−4505.

(31) Michel, T.; Debart, F.; Vasseur, J.-J.; Geinguenaud, F.; Taillandier, E. FTIR and UV Spectroscopy Studies of Triplex Formation between Alphaoligonucleotides with Non-Ionic Phosphoramidates Linkages and DNA Targets. *J. Biomol. Struct. Dyn.* **2003**, *21*, 435−445.

(32) Mergny, J.-L.; Lacroix, L. Analysis of Thermal Melting Curves. *Oligonucleotides* **2003**, *13*, 515−537.

(33) Becaud, J.; Pompizi, I.; Leumann, C. J. Propagation of Melting Cooperativity Along the Phosphodiester Backbone of DNA. *J. Am. Chem. Soc.* **2003**, *125*, 15338−15342.

(34) Jin, R.; Wu, G.; Li, Z.; Mirkin, C. A.; Schatz, G. C. What Controls the Melting Properties of DNA-Linked Gold Nanoparticles Assemblies? *J. Am. Chem. Soc.* **2003**, *125*, 1643−1654.

(35) Sun, Y.; Harris, N. C.; Kiang, C.-H. Melting Transition of Directly Linked Gold Nanoparticle DNA assembly. *Phys. A (Amsterdam, Neth.)* **2005**, *350*, 89−94.

(36) Qamhieh, K.; Wong, K.-Y.; Lynch, G. C.; Pettitt, B. M. The Melting Mechanism of DNA Tethered to a Surface. *Int. J. Numer. Anal. Modell.* **2009**, *6*, 474−488.

(37) Vainrub, A.; Pettitt, B. M. Coulomb Blockage of Hybridization in Two-Dimensional DNA Arrays. *Phys. Rev. E.* **2002**, *66*, 041905.

(38) Van Schooneveld, M. M.; Vucic, E.; Koole, R.; Zhou, Y.; Stocks, J.; Cormode, D. P.; Tang, C. Y.; Gordon, R. E.; Nicolay, Y.; Meijerink, A.; et al. Improved Biocompatibility and Pharmacokinetics of Silica Nanoparticles by Means of a Lipid Coating: A Multimodality Investigation. *Nano Lett.* **2008**, *8*, 2517−2525.

(39) Benyettou, F.; Lalatonne, Y.; Chebbi, I.; Di Benedetto, M.; Serfaty, J.-M.; Lecouvey, M.; Motte, L. Multimodal Magnetic Resonance Imaging Nanoplatform for Cancer Theranostics. *Phys. Chem. Chem. Phys.* **2011**, *13*, 10020−10027.

(40) Benyettou, F.; Chebbi, I.; Motte, L.; Seksek, O. Magnetoliposome for Alendronate Delivery. *J. Mater. Chem.* **2011**, *21*, 4813−4820.

(41) Motte, L.; Benyettou, F.; De Beaucorps, C.; Lecouvey, M.; Milesovic, I.; Lalatonne, Y. Multimodal Superparamagnetic Nanoplatform for Clinical Applications: Immunoassays, Imaging & Therapy. *Faraday Discuss.* **2011**, *149*, 211−225.

(42) Nikitin, P. I.; Vetoshko, P. M. Patent of Russian Federation RU 2166751, March 9, 2000, European Patent Application EP 1262766, March 7, 2001.

(43) Nikitin, M. P.; Torno, M.; Chen, H.; Rosengart, A.; Nikitin, P. I. Quantitative Real-Time in vivo Detection of Magnetic Nanoparticles by their Nonlinear Magnetization. *J. Appl. Phys.* **2008**, *103*, 07A304.